ARTICLE

Iron and steel corrosion mechanisms in a carbonate rich pore water: Multiscale characterization of the corrosion product layers

Hélène Lotz[1] 🄾 | Delphine Neff[1] | Florence Mercier-Bion[1] | Christian Bataillon[2] | Philippe Dillmann[1] | Emmanuel Gardes[3] | Isabelle Monnet[3]

[1]LAPA-NIMBE/IRAMAT, CEA/CNRS, Université Paris-Saclay, Gif-sur-Yvette, France

[2]CEA, Des—Service de Corrosion et de Comportement des Matériaux dans leurs Environnement (SCCME), Université Paris-Saclay, Gif sur Yvette, France

[3]Centre de Recherche sur les Ions, les Matériaux et la Photonique (CIMAP), CEA, CNRS, UCBN, ENSICAEN, Normandie Université, Caen, France

Correspondence
Hélène Lotz, LAPA-NIMBE/IRAMAT, CEA/CNRS, Université Paris-Saclay, Gif-sur-Yvette, France.
Email: lotz.helene.lucie@gmail.com

Abstract

Corrosion experiments were performed on a ferrito-pearlitic (P285-NH) and a ferritic steel (Armco) in a synthetic solution representing the Callovo-Oxfordian porewater during a month at 120°C. Corrosion product layers (CPLs) were characterized from micro to nanoscale in terms of morphology (electron microscopies), composition (energy dispersive X-ray spectroscopy), and structure (μ-Raman, selected area electron diffraction). Both systems present a Ca-siderite bilayer which interface locates the metal original surface, and nano to micrometric magnetite islets on the internal carbonated layer and at the M/CPL interface. The impact of cementite is highlighted in terms of morphology of the CPL and corrosion mechanism.

KEYWORDS
cementite, iron, magnetite, sidetire, steel

1 | INTRODUCTION

In anoxic water, corrosion involves metal oxidation into cations and proton reduction into dihydrogen. Interactions between metallic cations with ions from the environment induce the formation of corrosion product layers (CPLs). For steel in carbonated environments, siderite ($FeCO_3$) CPL was identified. In fairly intuitive way, such CPL should protect steels against long-term corrosion. In oil and gas industry,[1] buried archeological artifacts,[2,3] or geological storage for high-level radioactive waste,[4,5] such protection against corrosion has been evidenced with time-decreasing corrosion rates with the consequence of the growth of thick layers (>μm). This mechanism contrasts with that of steel passivation where the thickness of the layer is rather nanometric and consists in iron oxides. Iron passivation is well documented in literature for about five decades. A large number of experimental techniques have been used to characterize the passive layer from the macroscopic scale to the nanoscale in aqueous solutions[6–11] and specifically in carbonate media.[12–19] Particularly in carbonate media, despite several studies dealing with the condition of formation of the siderite layer,[20–24] the mechanisms of its protective role are not completely deciphered, including the influence of some parameters on the behavior of the system.

The present study focuses on this siderite CPL formed in the specific context of the geological storage for

radioactive waste. In France, the Callovo-Oxfordian (Cox) formation has been chosen for the high-level radioactive waste disposal.[25] Horizontal tunnels will be drilled in the Cox formation with a steel liner to prevent the collapse of the host rock. The disposal is based on a multi-barrier system where the radioelements are embedded in a glass matrix itself cast into a thin stainless-steel canister introduced into a low-alloyed steel overpack. The interaction between the overpack as well as the liner with the Cox environment will produce siderite containing CPL on low alloyed steels which will influence their corrosion rate. The influence of the microstructure comparing α-Fe and carbon steel has been barely studied previously in such corrosion conditions. Nevertheless, the nature of the carbon steel and especially the presence of cementite in the microstructure could have drastic effect on the behavior of the CPL.[26–31] To highlight the differences and similarities between the CPLs for these two types of steel, morphological and chemical characterizations have been performed on the Armco® (α-Fe) iron and on a pipeline steel (P285-NH) in the early stage of corrosion (1 month). To be in similar but accelerated conditions to storage that will be at 90°C, the temperature of 120°C was chosen.

After a brief depiction of samples and experiments, fine descriptions of the morphology and the nature of CPLs, in the early stages of corrosion in a synthetic Cox pore water, are given in the experimental results section. Finally, an attempt to link the microstructure of the CPLs with the anodic and cathodic steps of the corrosion is discussed focusing on the location of these elementary electrochemical processes.

2 | MATERIALS AND METHOD

2.1 | Samples

Two types of metallic substrates, a ferrito-pearlitic steel (P285-NH) and a pure ferrite (Armco), were used in the study, and their elemental compositions are given in Table 1. Metallographic Nital attack revealed their microstructures as shown in Figure 1. The ferrito-pearlitic steel is a mix of ferrite and pearlite grains, a succession of Fe_3C and α-Fe lamellas, while the ferrite sample is only made of ferrite grains.

Before the corrosion experiment, coupons were polished with SiC papers (from 800 down to 4000 mesh) using ethanol as lubricant. Between each polishing paper, samples were put in an ethanol beaker and placed 2 min in an ultrasonic bath to remove loose SiC grains. After the corrosion experiments and before analyses, samples were embedded in epoxy resin (EpoFix, Struers) and then cut with a precision diamond saw (Minitom, Struers). The cross-sections were ground with SiC paper (up to grade 4000) under ethanol and then polished with 1/4 μm diamond paste on a velvet disk.

2.2 | Corrosion experiments

The corrosion experiments were performed in an autoclave at 120°C during 1 month for all the samples. They were immersed in a synthetic solution representative of the Cox pore water in equilibrium with Bure argillite according to Gaucher et al.[32] The closest possible pore water chemical composition was chosen; namely the composition at 90°C calculated in Gaucher et al.[32] because no composition at 120°C is available to date (Table 2).

Once the coupons immersed, the autoclave was placed under a primary vacuum to remove air. A pressure of 3.3 bar of CO_2 was then added ($P(CO_2)_{eq}$ = 0.5 bar) followed by an additional pressure of 1 bar of helium to prevent boiling of the solution. Upon stopping the experiment, the samples were dried using a stream of dry air and then stored under primary vacuum.

After 1 month at 120°C in the synthetic Cox pore water, the CPL of both ferritic and ferrito-pearlitic samples were characterized from micrometric to nanometric scale.

### 2.3 | Analytical techniques

2.3.1 | Optical microscopy

Optical microscopy was used to provide initial information on the morphology and thicknesses of the CPL. Bright-field images were made using an Olympus BX51 microscope with an X50 objective. Optical micrographs were acquired under the open-source Micro-Manager

TABLE 1 Chemical composition of the low-alloy carbon steel used in the corrosion experiment (wt.%)

Elements	C	Si	Mn	S	P	Cr	Mo	Ni	Cu	Fe
P285-NH	0.15	0.25	1.03	0.001	0.006	0.081	0.021	0.067	0.073	Base
ARMCO	0.002	0.009	0.33	0.019	0.005	-	-	-	0.03	Base

FIGURE 1 Scanning electron microscopy micrographs of the metallic surface after metallographic attack. (a) Ferrito-pearlitic steel P285-NH (0.15 wt.%. C) and (b) pure ferrite Armco.
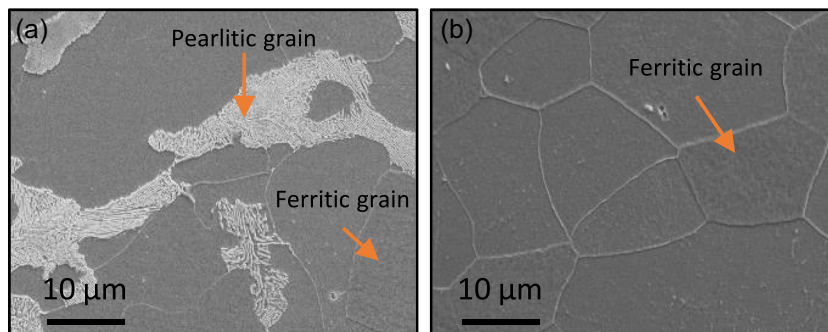
TABLE 2 Chemical composition of Bure synthetic solution in equilibrium with Bure argillite at 90°C[32]

	Na_2SO_4	KCl	$CaCl_2$	$MgCl_2$	$SrCl_2$	NaCl	Na_2SiO_3	$NaHCO_3$
C (mmol L^{-1})	10	0.96	10	2.5	0.14	14.7	0.84	2.62

software with a Nikon D600 camera controlled by the NK-Remote software.

2.3.2 | Scanning electron microscopy-energy dispersive spectroscopy (SEM-EDS)

The morphology and chemical composition of the corrosion layers were investigated using a field emission gun-scanning electron microscope (JEOL SEM 7001F). Surfaces and cross-sections of the samples were observed in secondary electron (SE) and backscattered electron (BSE) modes. The SEM is coupled to a silicon drift detector to investigate elemental composition by energy dispersive X-ray spectroscopy (EDX). Analyses were performed at 10 kV accelerating voltage and with a probe current of about 3 nA. The acquisition and data treatment (local composition analyses and composition maps) were performed using Aztec software developed by Oxford Instruments.

2.3.3 | μ-Raman spectroscopy

μ-Raman analyses were performed with a Renishaw Invia Reflex spectrometer equipped with a doubled Nd:YAG laser emitting at 532 nm and a microscope to focus the beam on the surface. The spectrometer was calibrated in energy with a silicon wafer (reference peak at 520 cm^{-1}). The analyses were carried out with a beam intensity of the order of a few 100 μW to avoid the transformation of the analyzed phases under laser heating. CPL was investigated with surface mapping. The spectral information was acquired during 20 s on each point with a step of 0.75 μm to overlap each point and enhance the spatial resolution (beam size of 1.2 μm).

Mapping data processing includes cosmic peak removal with the Cosmic Ray Remover add-on included in WIRE software pack. The following steps were carried out using functionality incorporated in a homemade software, Multicorr, developed at the LAPA and including several multivariate functionalities.[33] First, asymmetric least squares were performed for the baseline correction of the spectra. The spectra were normalized (total area of each spectrum). Then, data treatment was completed with principal component analyses (PCA), followed by a clustering allowing to (i) remove the signal corresponding to the metal and to the resin, (ii) filter the noise, and (iii) locate the different structural phases in the map.

2.3.4 | Focused ion beam-SEM (FIB-SEM) and scanning transmission electron microscopy (STEM)

Thin sections (~100 nm thickness) were extracted from the samples prepared as cross sections using the scanning electron microscope coupled with focused Ga-ion beam FEI Nanolab 660 of CIMAP. Lamella thinning was performed first using 30 kV Ga ions, followed by final polishing at decreasing energies of 5, 2, and 1 kV to remove possible Ga$^+$ implantation and damages.[34] The thin sections were then stored in sealed jars under vacuum. Preliminary observations have been performed at 30 kV using the retractable STEM detector installed in the FIB-SEM.

2.3.5 | Transmission electron microscopy (TEM)

Nanometric chemical and structural information was obtained using the TEM JEOL 2010 F of IRMA (Caen)
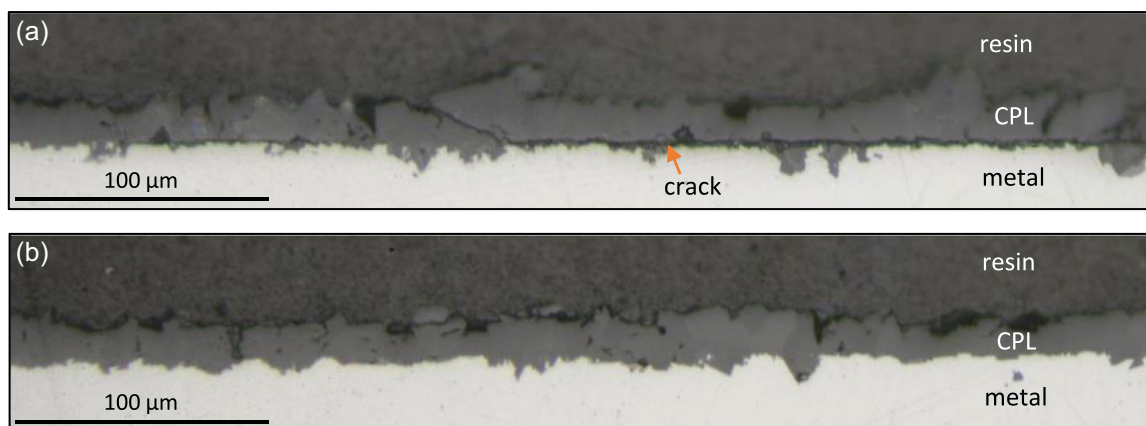
FIGURE 2 Global morphology of (a) the ferrito-pearlitic and (b) the ferritic samples as cross-sections (optical microscopy).

and equipped with a diode EDAX X-ray microanalysis. Analyses were operated at 200keV. Phase identification was performed using selected area electron diffraction (SAED). Radial intensity profiles were obtained using the "locate selected area diffraction pattern centre" function in manual mode and the "rotational average" function from the DiffTool package inside Digital Micrograph software.[35] Interplanar d-spacing was compared to the diffraction data d_{hkl} from Joint Committee on Powder Diffraction Standards (JCPDS) files. To localize some specific phases, dark field images were acquired.

3 | RESULTS

Optical micrographs acquired of the ferrito-pearlitic and the ferritic cross sections show their CPL morphology (Figure 2).

For the ferrito-pearlitic sample (Figure 2a), the CPL presents an almost continuous crack at the metal/CPL interface. On the contrary, the CPL of the ferritic sample (Figure 2b) appears well adherent to the metal. Additionally, CPL thicknesses were measured on about 50 SEM images for each sample. They range from 10 to 60 μm (mean value of 21 μm) for the ferrito-pearlitic sample while for the ferritic sample, values range from 10 to 37 μm (mean value of 18 μm). The CPL thickness of the ferrito-pearlitic sample appears slightly more heterogeneous than for the ferritic one, although there is no significant difference of the corrosion thickness mean value for the two samples (Figure 3).

BSE-SEM micrographs of the two corroded samples P285-NH and Armco were acquired to observe the density contrast of the different phases present in the CPL (Figure 4). These observations were completed with EDX analysis showing that the CPL contained oxygen, iron, and calcium. For the P285-NH corroded sample
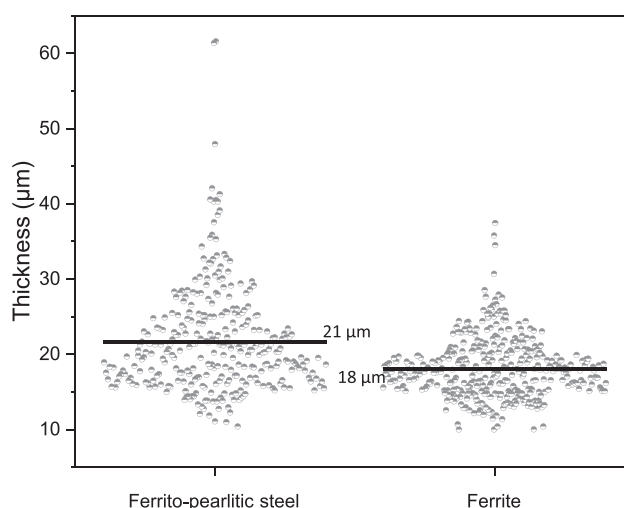

FIGURE 3 Corrosion product layer thicknesses for the ferrito-pearlitic and the ferritic samples. The black line corresponds to the average of the measured values (P285-NH: 311 measurements on 56 images, Armco: 383 measurements on 54 backscattered electron-scanning electron microscopy images).

(Figure 4a), ghost grains of cementite were observed. Therefore, the α-Fe phase was corroded contrary to the cementite Fe_3C that was not corroded and appeared as white lamellas. Thus, the location of cementite can be considered as a position marker of the original surface of the coupon before the corrosion experiment. For the Armco corroded sample such marker did not exist. For both samples, the CPL presented a homogeneous dark gray matrix. Locally, brighter islets analyzed by EDX and containing Fe and O only, appeared at the metal/CPL interface with micrometric to submicrometric sizes. In addition, some darker islets with micrometric thickness were located inside the CPL at the vicinity of the original surface. From EDX Ca maps, these darker islets were enriched in calcium. For the ferritic sample, the location
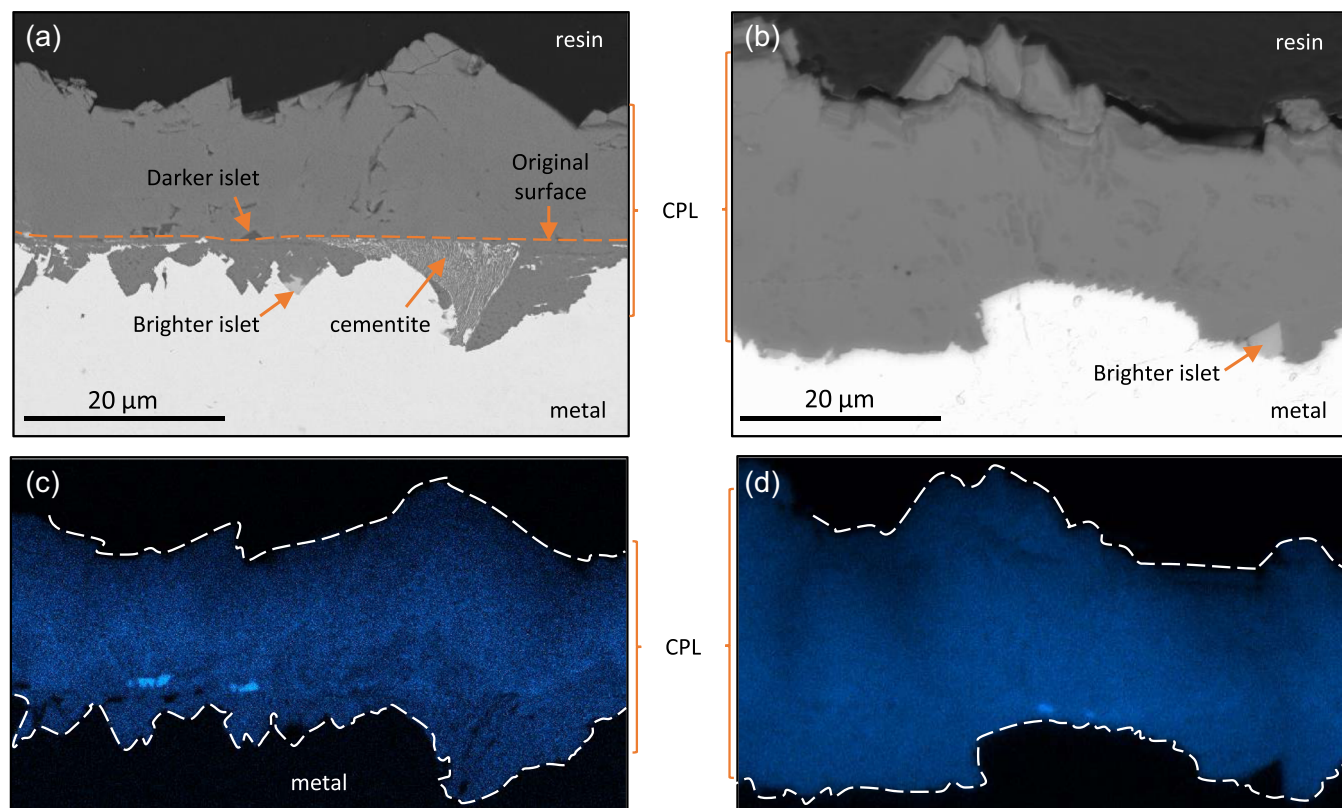
FIGURE 4 Observation in cross-section of the corrosion product layer of (a) the P285-NH and (b) the Armco samples (backscattered electron-scanning electron microscopy images). (c) and (d) respective associated calcium mapping (energy dispersive X-ray spectroscopy).

of the original surface is not determined at this stage of analyses.

The areas observed by SEM-EDX were mapped using Raman spectroscopy to identify the crystalline structure of the different phases. PCA was used to identify the areas with the same spectral information (see methodological part).

The first main component (PC1) highlighted a strong peak at $1081 \, cm^{-1}$ and a weaker at $280 \, cm^{-1}$ consistent with carbonate structure (Figure 5). Thus the combination of the chemical and structural data, allowed to confirm that the corroded matrix consisted mainly of siderite (rich in Ca and Mg[36]).

The projection of PC1 on the map showed that the carbonated components were present throughout the whole corroded matrix and corresponded to the homogeneous dark gray matrix observed by BSE-SEM. However, the intensity of this projection varies between the internal area and the external one (Figure 6), with a lower intensity of the summed Raman spectra of the internal zone compared to the external one.

The difference in Raman signal intensity of the siderite carbonate bands in the iCP and eCP might be related to several parameters including the grains size (siderite grains bigger in the eCP than iCP), the
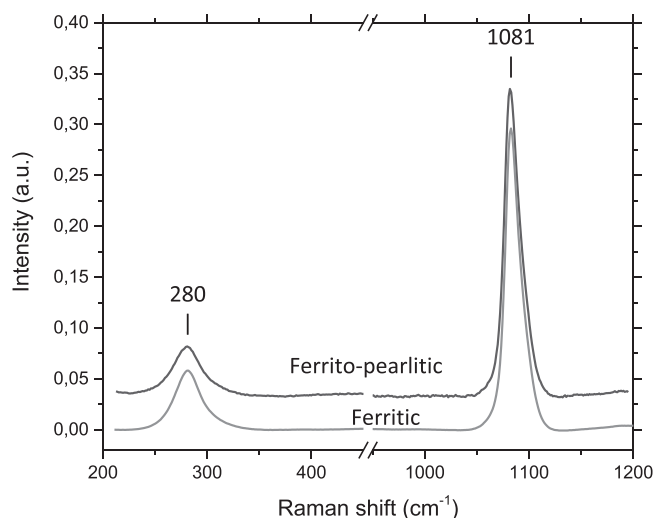
FIGURE 5 Spectral representation of the first principal component highlighting a carbonated structure, Raman spectroscopy.

degree of crystallinity of siderite (eCP more orderly than iCP), the concentration or detectability of the phase (signal reduced in the iCP due to the proximity with the metal and/or the presence of other elements in the layer).[37]
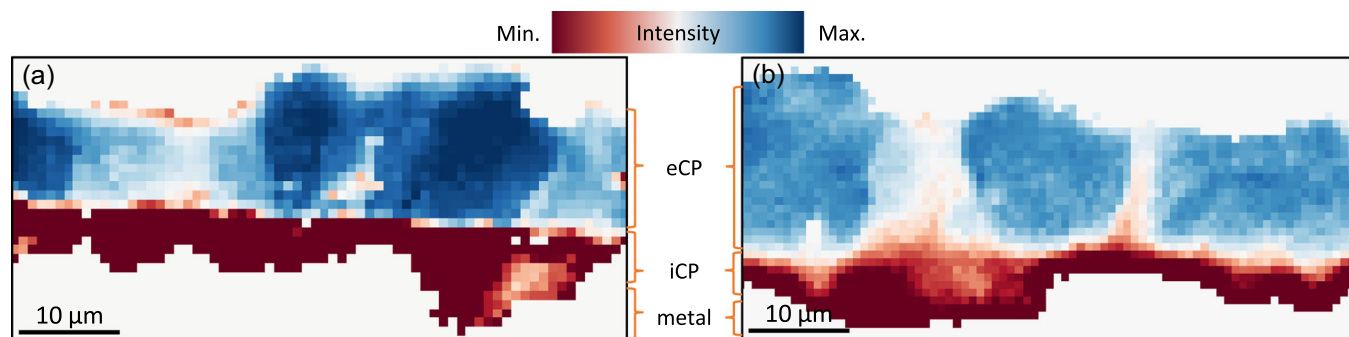
FIGURE 6 Projection of the first principal component (PC1) for (a) the ferrito-pearlitic and (b) the ferritic sample, Raman spectroscopy.
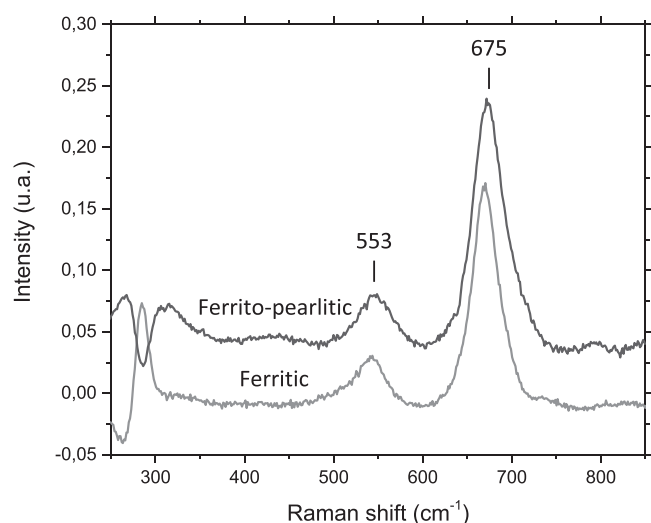

FIGURE 7 Spectral representation of the second principal component (PC2) characteristic of magnetite for the ferrito-pearlitic and the ferritic samples, Raman spectroscopy.

Thereby, the carbonate matrix can be divided into two parts: an internal CPL (iCP), in contact with the metal, and an external corrosion product one (eCP). This division in two sublayers is consistent with the location of the original surface for the ferrito-pearlitic sample identified previously by the presence of cementite. The location of the original surface at the interface between iCP and eCP was assumed similar to the ferritic sample. This will be commented in the discussion.

The spectral representation of the PC2 presented in Figure 7 contained an intense peak at $675 \, cm^{-1}$ and a peak with medium intensity at $553 \, cm^{-1}$ which highlighted the presence of magnetite.[38]

In addition, the projection of the PC2 on the map, presented in Figure 8, showed the correlation between the brighter islets observed by BSE at the M/CPL interface and the presence of this phase.

The microstructures of both iCP and eCP were investigated at nanoscale on thin section of the samples by STEM and TEM. For both samples, the metal, the iCP,

and the eCP layers are present on the thin sections of the STEM dark field images shown in Figure 9. For P285-NH sample, the iCP layer contained substantial pores ranging from 20 to 100 nm in diameter with additional brighter islets (Figure 9a). The iCP and eCP layers are separated from each other. For Armco sample, the iCP layer has less porosities compared to P285-NH sample at this observation scale. The few pores visible in Figure 9b were about 20 nm in diameter. Brighter islets are also observed in the iCP of Armco sample. The iCP and eCP layers seemed to adhere well to each other. This is in good correlation with the difference of Raman intensity signal marking the iCP/eCP front with a higher intensity of the siderite signal for the larger grains (Figure 10).

Electronic diffraction obtained by TEM/SAED confirms the presence of magnetite-maghemite at nanoscale. Diffraction patterns were acquired on the brighter micrometric islets at the M/CPL interface of both samples identified previously as magnetite. Comparison of the d-spacing 2.9, 2.0, and 1.4 Å, present on the diffraction patterns with PDF files of iron, iron carbonate, and iron oxide, confirms the presence of maghemite/magnetite iron oxide type. Although the distinction between maghemite and magnetite is difficult on such diffractogram, this result is coherent with the results obtained by μ-Raman spectroscopy.

In a second step, dark field images were acquired by positioning the objective aperture on the d-spacing of 2.9 Å of magnetite-maghemite pattern. Consequently, all the crystallites having the same orientation as the diffracted crystallite appeared brighter in the dark field images in Figure 11. For the P285-NH, the bright areas corresponded to an islet of a few nanometers to around 1 μm thick at the metallic interface as well as submicrometric to nanometric islets in the internal siderite layer. For the Armco sample, the dark field images highlight a close distribution of bright islets with submicrometric islets at the interface between the internal and external layers of siderite as well as nanometric islets (about 4–6 nm thick) at the metallic interface.
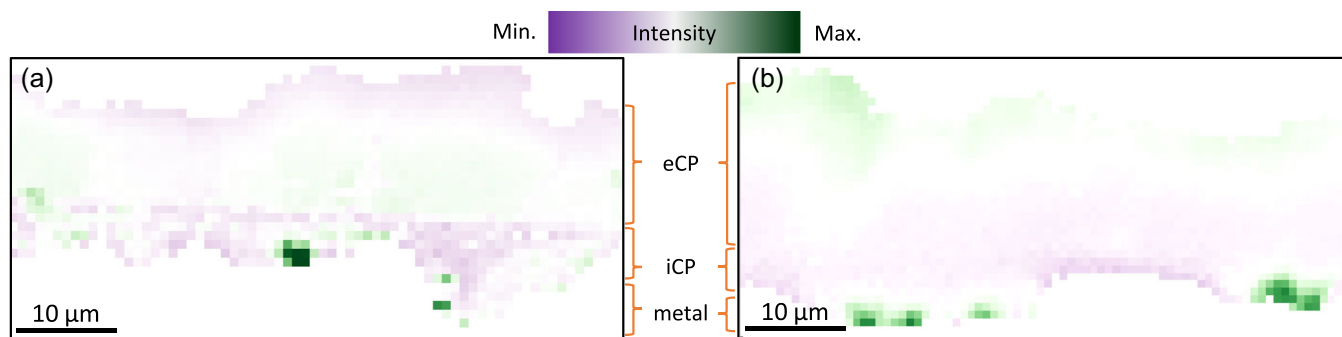
FIGURE 8 Projection of the second principal component (PC2) for (a) the ferrito-pearlitic and (b) the ferritic samples, Raman spectroscopy.
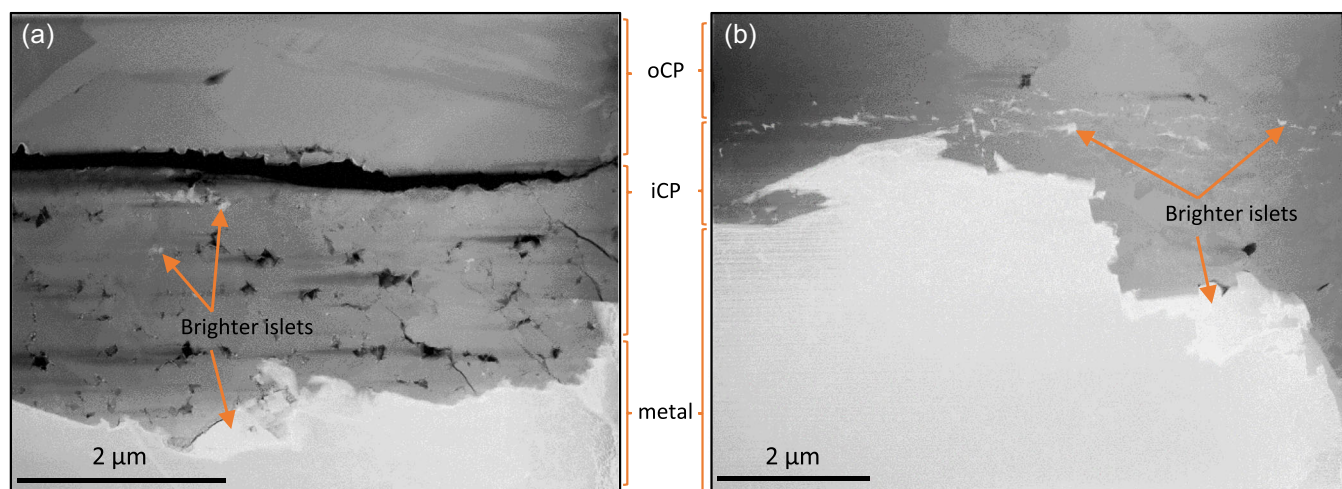
FIGURE 9 Observations of thin sections taken from the corrosion product layer of (a) P285-NH and (b) Armco samples (scanning transmission electron microscopy HAADF).

4 | DISCUSSIONS

Figure 12 sums up the characterization results obtained on the two systems. For the two steel grades, the composition and structure of the CPL appear very similar. They are composed of a bilayer of siderite enriched in calcium (10 wt.%) and magnesium (1 wt.%), with magnetite islets on the internal layer and calcite islets at the metal original surface.

Calcite islets are located on the external side of the original surface, suggesting that this mineral precipitated first on the uncorroded surface. This phenomenon has been highlighted by Esmaeely et al.[39] during the first day of an experiment conducted at 80°C by measuring the saturation ratio of calcite that stabilizes after 2 days. After this period, the saturation ratio of siderite increases due to the corrosion of the metal and the increase in the concentration of the Fe^{II} ions in solution. This induces change in the thermodynamic conditions favorable to the precipitation of siderite.

4.1 | Ca-siderite

For both samples, the carbonate matrix precipitates with a certain amount of calcium in their crystalline structure. This observation was also performed by Zhao et al.[40] and Gao et al.[20] who identified the formation of a siderite bilayer containing calcium in an anoxic carbonate medium. The presence of calcium in the siderite matrix has also been reported in studies achieved on archeological analogs[41] (5 wt.%) and laboratory experiments[42–48] (10 wt.%) in the field of radioactive waste storage. This divalent cation replaces Fe^{2+} cations in the structure while maintaining a rhombohedral configuration. Railsback[49,50] noted that the presence of calcium, up to a certain amount, in the siderite structure induces a better stability of the compound (log K_{sp} (25°C) = −11.4 for ankerite FeCaCO$_3$, −10.4 for siderite FeCO$_3$, and −8.5 for calcite CaCO$_3$).

As observed by Esmaeely et al.[24] and Rizzo et al.,[51] the quantity of divalent cations in solution, in particular for Ca^{2+}, can affect the elemental composition of the
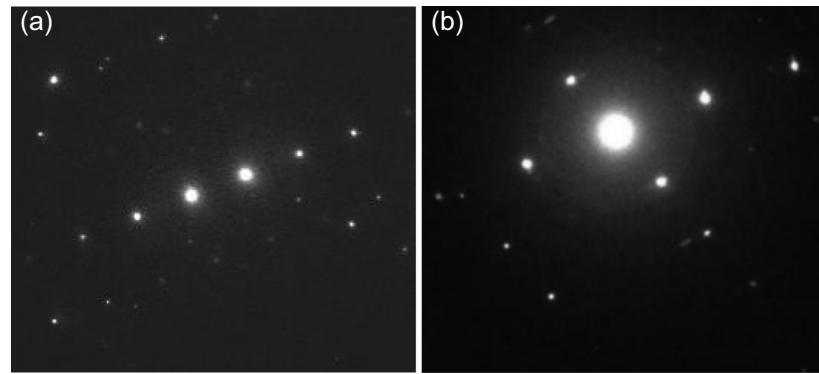
FIGURE 10 Electronic diffractogram obtained by selected area electron diffraction on the micrometric islets: (a) the ferrito-pearlitic and (b) the ferritic samples. (c) Radial intensity profile from selected area diffraction pattern with d-spacing characteristic of magnetite-maghemite iron oxide.
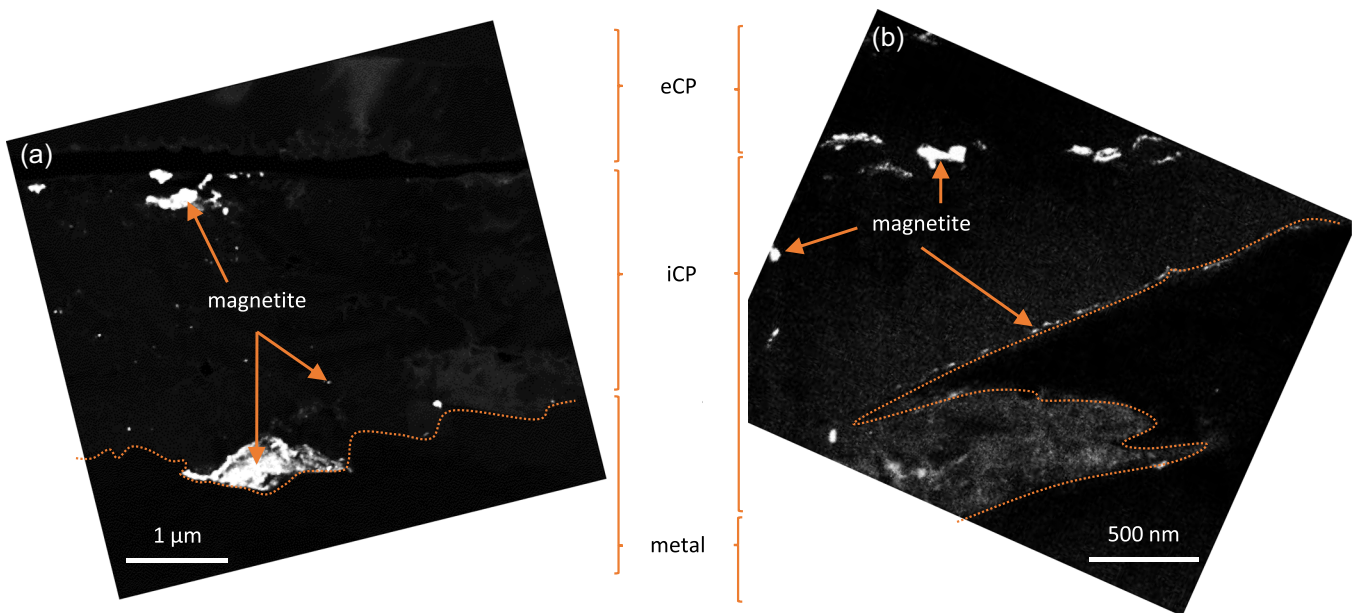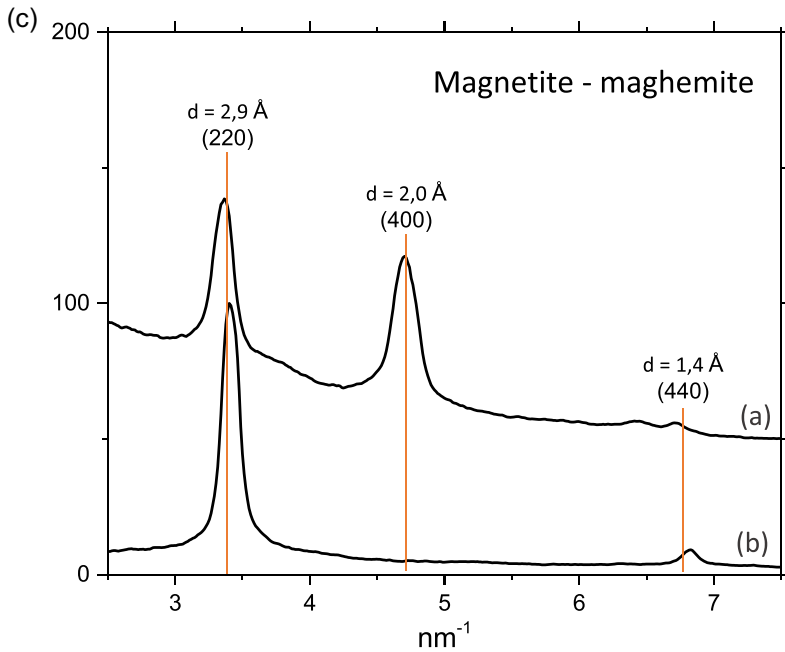
FIGURE 11 Location of nanometric to micrometric islets of magnetite in the corrosion product layer (CPL) of (a) the ferrito-pearlitic and (b) the ferritic samples. The orange discontinuous lines correspond to the M/CPL interface. Darkfield transmission electron microscopy orientation images were obtained by positioning the aperture of the objective on a magnetite diffraction spot.
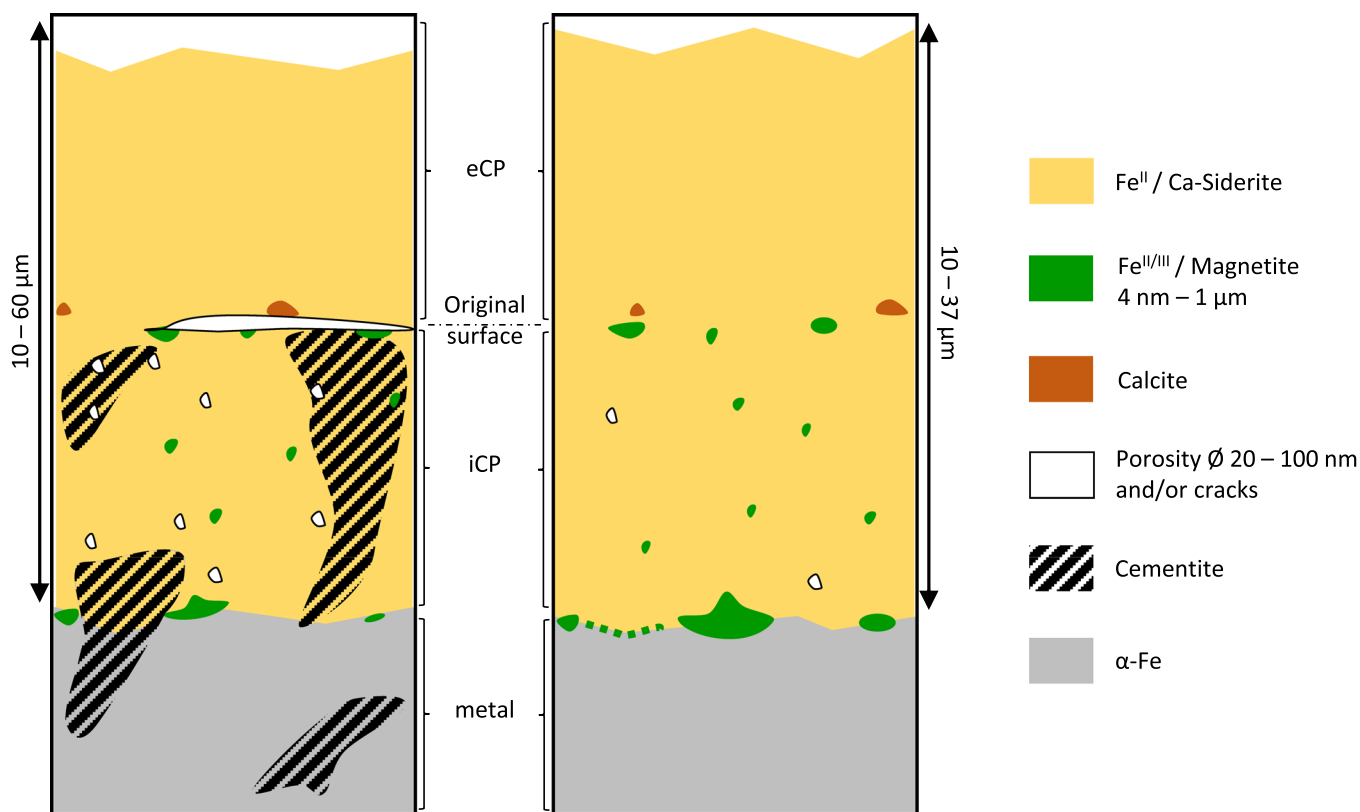
FIGURE 12 Schematic diagram of the corrosion forms observed on (left) the ferrito-pearlitic steel and (right) on the ferritic samples

carbonate layer and its stability properties. Indeed, experiments they performed on a 1Cr steel in a 1 wt.% NaCl solution at 80°C with CO_2 permanent flux and different concentrations of Ca^{2+} (0, 100, 1000, 10 000 ppm) evidenced (i) no change in the electro-chemical measurement with 0 and 100 ppm of Ca^{2+}, (ii) a drop in corrosion potential correlated with an increase of the corrosion rate up to 1000 ppm, and (iii) modification of the carbonate grains morphology on the substrate up to 10 000 ppm. Thus, the corrosion rate is linked to the chemical properties of the carbonate grains that precipitate on the surface of the metallic substrate. In the study presented here, calcium is present in the initial corrosion medium at 10 mmol L^{-1}, that is, approximately 400 ppm. CPL is made of leaf-like grains of regular size composed of Fe/Ca carbonate with iron as the major element (~10 wt.% Ca). The chemical properties of the carbonate layers match those that allow this layer to act as a diffusion barrier.

The pH, P (CO_2), and temperature factors should also be considered in the precipitation of carbonate layers. Dugstad et al.[52] noted that above 80°C, the decreasing corrosion rate is mainly correlated to the temperature increase, the pH, and the P(CO_2) having a lower impact on the corrosion processes. Indeed, the siderite solubility product constant K_{sp} decreases with increasing temperature. The siderite precipitates faster and its diffusion barrier property will take place earlier.[53] In our study, the temperature of 120°C will therefore play a role in the property of the carbonate matrix to reduce the corrosion rate.

4.2 | Bi-layer structure

Both systems present a bi-layer pattern, named in this paper iCP and eCP for internal and external corrosion layer respectively. In addition, in the ferrito-pearlitic system, the presence of non-corroded cementite merely in the iCP strongly suggests that the initial original metallic surface of the sample is located between the iCP and the eCP. The same hypothesis can be extrapolated to the ferritic system, because of comparable features between iCP and eCP in both systems: a low Raman signal intensity of carbonate bands completed with the presence of magnetite nano islets for the iCP and high Raman signal intensity of carbonate band for the eCP.

Thus, while the metal corrodes, part of Fe^{2+} ions precipitates with calcium and carbonate ions to form the iCP, a Ca-siderite layer replacing the volume initially occupied by the ferrite. In the meantime, the excess of Fe^{2+} ions precipitates on the external surface, forming the eCP.

4.3 | iCP

The main differences between the ferrito-pearlitic and the ferritic system are located in this iCP. While both systems contain magnetite grains in the whole iCP as well as at the M/CPL interface, the first one contains additional non-corroded cementite in the whole thickness of the iCP complemented with a higher density and sizes of porosities compared to the ferritic system.

The presence of magnetite at the interface was observed and discussed by several papers.[21,54,55] It was explained by a pH increase due to the production of OH^- ions (or consumption of H^+) through the cathodic reaction of metal corrosion at this location. Yet a study by De Motte et al.[21] have measured the increase of pH inside an ongoing growing layer of siderite at 80°C. The authors observed a variation of several 0.1 to 1 unit of pH. This is sufficient in some conditions to switch from the predominance domain of siderite to the one of magnetite. This could be the case for the ferritic system. Nevertheless, for the ferrito-pearlitic system, the presence of cementite lamellas, a conducting phase connected to the metal, strongly suggests a decoupling of anodic and cathodic reactions. This tends to discard the hypothesis of pH increase at this location by the effect of the cathodic reaction. Then, another hypothesis, based on kinetics considerations can be proposed to explain the stability of magnetite at the metal iCP interface in case of galvanic coupling. As said before, De Motte et al.[2] have observed the same kind of magnetite precipitates (see fig. 19 in De Motte et al.[55]) on API5L X65 corroded in carbonated solution at 80°C. During this study, corrosion monitoring has shown that the corrosion rate was decreasing and that the potential slowly shifted in the anodic direction for about 8 days (see Figure 11b in Turgoose et al.[2]). From literature, it is well-known that cementite is an efficient cathode phase.[56] Thus, as said before, the reduction of oxidant is mainly located at the surface of cementite whereas the oxidation of steel is located at the surface of α–Fe matrix. So, this electrochemical system runs as a local micro-cell. To close it, an ionic current, which could be a blend of anionic and cationic currents, must cross the iCP, building a voltage drop in this iCP. Therefore, the electrochemical potential drops at the anode and cathode interfaces are different as depicted in Figure 13.

The growth of iCP layer likely induces a time decrease of the corrosion rate j_{corr} and so an increase of the electrochemical potential E_c. However, if the decrease of the corrosion rate was slower than the increase of the equivalent ionic resistance of the iCP then the voltage drop ΔE can increase (see Figure 14) so shifting the electrochemical potential E_a in anodic direction. Then, the consequence of the anodic shift of E_a could be an increase in the release of ferric ions compared to ferrous ions in solution at the metal/CL interface. This could explain the local precipitation of magnetite since the amount of ferric cations would be too high to precipitate siderite.

From EIS data, De Motte et al. have also shown that the electroactive surface was decreasing down to about zero (see Figure 12 in De Motte et al.[55]). This corresponds to a clogging of the iCP with a likely increase in the ionic resistance of the iCP layer. It is believed that the coupling effect between cementite and α-Fe matrix could be more likely an explanation.

The presence of nanometric pores in the iCP of the ferrito-pearlitic steel could also be linked to the decoupling effect of the cathodic reactions all along the cementite lamellas.[26,27,31] This reaction could cause the production of H_2 along the cementite due to a higher corrosion kinetic induced by a rapid electron flux. This could induce the formation of pores inside the corrosion layer. However, two counterarguments weaken this hypothesis. First, it can be questioned why the pores could not be clogged by further precipitation of siderite while the corrosion progressively consumes the metal and release Fe^{2+} ions in solution. Second, their presence seems to be quite homogeneously distributed inside the iCP indicating that their formation is independent of the corrosion rate. At this stage, the presence of porosity in the ferrito-pearlitic system proved to be difficult to explain.

These considerations suggest that the presence of cementite in the ferrito-pearlitic steel, leading to the decoupling of reactions, conducts to a specific mechanism that seems to be different from the one that takes place in the purely ferritic systems for which the magnetite precipitation is more probably linked to a pH increase. Nevertheless, it should be noted that the average corrosion rates of the two systems are relatively the same when one considers the thickness of the corrosion products (18 μm vs. 21 μm for ferrio-pearlitic and ferritic systems respectively). This similarity does not imply that the instantaneous corrosion rate was constantly the same for the two systems. Important observations were made on some corrosion systems formed on archeological ferritic artifacts corroded in a carbonated environment on which a siderite layer formed, showing the possible decoupling of the anodic and cathodic reactions in such corrosion layers. First magnetite islets embedded inside the siderite matrix were proven to be electrically connected to the metal thanks to C-AFM analyses.[57] Second copper tracing experiments have shown the precipitation of metallic copper inside the corrosion during a recorrosion experiment conducted in a copper salt solution proving the possible transport of electrons inside a carbonate layer.[58] The electrical behavior of the layer formed on the ferritic system must consequently be studied more deeply in the future.
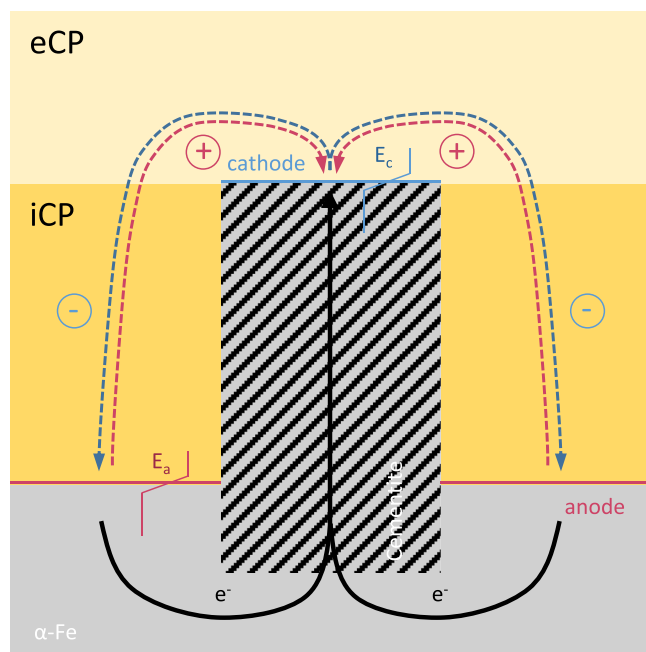
FIGURE 13 Schematic representation of an anodic cathodic coupling in P285-NH steel.
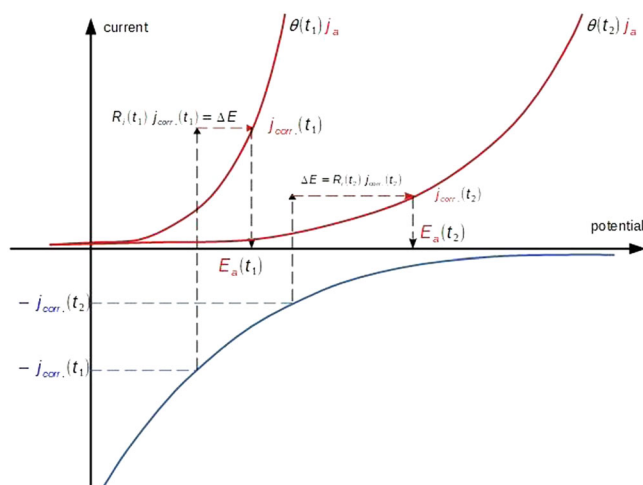
FIGURE 14 Coupling between the anodic and cathodic Butler–Volmer current-voltage curves for P285-NH steel. J_a anodic current, E_a anode potential, J_{corr} corrosion current, $\Delta E = E_a - E_c$, E_c cathode potential, $\theta(t_1) > \theta(t_2)$ electroactive anodic surfaces decreased because of the clogging of iCP.

5 | CONCLUSION

Both ferritic and ferrito-pearlitic samples seemed to behave similarly after 1 month of corrosion in a carbonate environment. Both samples exhibit a Ca-siderite bilayer that forms on either side of the original metal surface, with a chemical property in favor of a reduction in the rate of corrosion. In addition,

nanometric to micrometric islets of magnetite were identified on the internal Ca-siderite layer of both systems.

Nanoscale observations of the internal layer of Ca-siderite question the dependence of corrosion mechanisms on the microstructure of the metal substrate after 1 month of corrosion. Indeed, the presence of non-corroded cementite lamellas with conductive properties inside the iCP of the ferrito-pearlitic sample can induce a delocation of the cathodic reaction inside the CPL. This questions the ability of the ferritic system to mimic the ferrito-pearlitic system, or to evolve through a completely different corrosion mechanism compared to the ferrito-pearlitic system.

This study shows the importance of comparing the influence of the metal microstructure on the evolution over longer durations of the corrosion of the two systems.

DATA AVAILABILITY STATEMENT

The data that support the findings of this study are available from the corresponding author upon reasonable request.

ORCID

Hélène Lotz http://orcid.org/0000-0002-9372-8695

REFERENCES

[1] T. E. Perez, *JOM* **2013**, *65*, 1033.
[2] S. Turgoose, *Stud. Conserv.* **1985**, *30*, 13.
[3] H. Matthiesen, L. R. Hilbert, D. Gregory, B. Sørensen, *EUROCORR—European Corrosion Conference: Long Term Prediction and Modelling of Corrosion 20041–12*, 2004.
[4] D. Feron, D. D. Macdonald, Prediction of Long Term Corrosion Behaviour in Nuclear Waste Systems. *Materials Research Society Symposium Proceedings*, **2006**, Vol. *932*, pp. 1–6.
[5] D. Féron, D. Crusset, J.-M. Gras, *J. Nucl. Mater.* **2008**, *379*, 16.
[6] B. MacDougall, M. Graham, in *Corrosion Mechanisms in Theory and Practice*, 2nd ed. (Ed. P. Marcus), Marcel Dekker, Inc., New York **2002**, p. 190.
[7] G. T. Burstein, G. W. Ashley, *Corrosion* **1984**, *40*, 110.
[8] L. J. Oblonsky, A. J. Davenport, M. P. Ryan, H. S. Isaacs, R. C. Newman, *J. Electrochem. Soc.* **1997**, *144*, 2398.
[9] A. J. Davenport, L. J. Oblonsky, M. P. Ryan, M. F. Toney, *J. Electrochem. Soc.* **2000**, *147*, 2162.
[10] L. J. Oblonsky, M. P. Ryan, H. S. Isaacs, *Corros. Sci.* **2000**, *42*, 229.
[11] K. Ritter, M. S. Odziemkowski, R. W. Gillham, *J. Contam. Hydrol.* **2002**, *55*, 87.

[12] D. H. Davies, G. T. Burstein, *Corrosion* **1980**, *36*, 416.

[13] E. B. Castro, J. R. Vilche, A. J. Arvia, *Corros. Sci.* **1991**, *32*, 37.

[14] J. K. Heuer, J. F. Stubbins, *Corros. Sci.* **1999**, *41*, 1231.

[15] J. Han, *Galvanic Mechanism of Localized Corrosion for Mild Steel in Carbon Dioxide Environments*, Ohio University, **2009**.

[16] R. De Marco, Z.-T. Jiang, B. Pejcic, E. Poinen, *J. Electrochem. Soc.* **2005**, *152*, B389.

[17] R. De Marco, Z.-T. Jiang, D. John, M. Sercombe, B. Kinsella, *Electrochim. Acta* **2007**, *52*, 3746.

[18] S. L. Wu, Z. D. Cui, F. He, Z. Q. Bai, S. L. Zhu, X. J. Yang, *Mater. Lett.* **2004**, *58*, 1076.

[19] C. T. Lee, Z. Qin, M. Odziemkowski, D. W. Shoesmith, *Electrochim. Acta* **2006**, *51*, 1558.

[20] M. Gao, X. Pang, K. Gao, *Corros. Sci.* **2011**, *53*, 557.

[21] R. De Motte, R. Mingant, J. Kittel, F. Ropital, P. Combrade, S. Necib, V. Deydier, D. Crusset, *Electrochim. Acta* **2018**, *290*, 605.

[22] T. Tanupabrungsun, D. Young, B. Brown, S. Nešić, *NACE Corrosion 2012*, NACE, Houston 2012, Paper Number: NACE-2012-1418.

[23] R. Barker, D. Burkle, T. Charpentier, H. Thompson, A. Neville, *Corros. Sci.* **2018**, *142*, 312.

[24] S. N. Esmaeely, Y.-S. Choi, D. Young, S. Nešić, *Corrosion* **2013**, *69*, 912.

[25] E. Gaucher, C. Robelin, J. M. Matray, G. Négrel, Y. Gros, J. F. Heitz, A. Vinsot, H. Rebours, A. Cassagnabère, A. Bouchet, *Phys. Chem. Earth* **2004**, *29*, 55.

[26] D. N. Staicopolus, *J. Electrochem. Soc.* **1963**, *110*, 1121.

[27] K. Videm, J. Kvarekval, T. E. Perez, G. Fitzsimons, Surface Effects on the Electrochemistry of Iron and Carbon Steel Electrodes in Aqueous CO2 Solutions. In: *Proceedings of the CORROSION 96*, OnePetro, **1996**.

[28] S. Al-Hassan, B. Mishra, D. L. Olson, M. M. Salama, *Corrosion* **1998**, *54*, 480.

[29] J.-L. Crolet, N. Thevenot, S. Nesic, *Corrosion* **1998**, *54*, 194.

[30] J. Sánchez, J. Fullea, C. Andrade, J. J. Gaitero, A. Porro, *Corros. Sci.* **2008**, *50*, 1820.

[31] F. Farelas, B. Brown, S. Nesic, Iron Carbide and Its Influence on the Formation of Protective Iron Carbonate in CO_2 Corrosion of Mild Steel. In: *Proceedings of the CORROSION 2013*, OnePetro, **2013**.

[32] É. C. Gaucher, P. Blanc, F. Bardot, G. Braibant, S. Buschaert, C. Crouzet, A. Gautier, J.-P. Girard, E. Jacquot, A. Lassin, G. Negrel, C. Tournassat, A. Vinsot, S. Altmann, *C. R. Geosci.* **2006**, *338*, 917.

[33] R. Le Penglau, *Analyses Multivariées et Multiblocs d'images Hyperspectrales Pour La Prédiction de La Corrosion Sur Le Long Terme: Application à La Corrosion Atmosphérique d'alliages Ferreux Historiques*, Pierre et Marie Curie, **2017**.

[34] R. M. Langford, A. K. Petford-Long, *J. Vac. Sci. Technol., A* **2001**, *19*, 2186.

[35] D. R. G. Mitchell, *Microsc. Res. Tech.* **2008**, *71*, 588.

[36] M. Saheb, D. Neff, P. Dillmann, H. Matthiesen, E. Foy, *J. Nucl. Mater.* **2008**, *379*, 118.

[37] S. Guilhem, *Spectroscopies Vibrationnelles: Théorie, Aspects Pratiques et Applications*, Editions des archives contemporaines, **2020**.

[38] D. L. A. de Faria, S. Venâncio Silva, M. T. de Oliveira, *J. Raman Spectrosc.* **1997**, *28*, 873.

[39] S. Navabzadeh Esmaeely, Y.-S. Choi, D. Young, S. Nešić, *Corrosion* **2013**, *69*, 912.

[40] G. Zhao, X. Lu, J. Xiang, Y. Han, *J. Iron Steel Res. Int.* **2009**, *16*, 89.

[41] M. Saheb, *Les Analogues Archéologiques Ferreux Pour La Compréhension Des Mécanismes de Corrosion Multiséculaire En Milieu Anoxique, (thesis), Saclay*, **2009**.

[42] F. Martin, M. Fenart, C. Saclay, *Essais de Corrosion de Longue Durée En Argilite: Prélèvements à 7 Mois Rapport Intermédiaire CORRIDDA*, **2009**.

[43] M. Schlegel, C. Blanc, *Characterization of the Iron-Clay Corrosion Interface From Corridda Setups*, **2010**. NT DPC / SCP 10-371.

[44] M. Schlegel, C. Blanc, *Characterization of the Iron-Clay Interface of Corridda Samples Reacted for 27 Months*, **2012**. NT DPC / SEARS 12-426.

[45] F. Brucker, M. L. Schlegel, C. Blanc, *Characterization of the (Glass)-Iron-Clay Interface Reacted at 90°C for 24 Months: Arcorr-2008 Samples*, **2012**. NT DPC / SEARS 12-436.

[46] M. L. Schlegel, C. Bataillon, F. Brucker, C. Blanc, D. Prêt, E. Foy, M. Chorro, *Appl. Geochem.* **2014**, *51*, 1.

[47] M. L. Schlegel, J. Varlet, C. Blanc, *Corrosion at the Interface of Steel in Contact With Clay or in a Model Microcontainer: Results From the Final Corridda Samples (76 Months of Reaction)*, **2015**, pp. 1–41. NT DPC 15–007.

[48] M. L. Schegel, M. Sennour, C. Carrière, F. Martin, M. Fenart, J. Varlet, C. Blanc, P. Dillmann, D. Neff, J. J. Dynes, *Corrosion at the Steel-Clay Interface at 90 C: Nanoscale Characterization of Metal-Replacing Corrosion Products*, **2017**.

[49] L. B. Railsback, *Carbonates Evaporites* **1999**, *14*, 1.

[50] L. B. Railsback, *Some Fundamentals of Mineralogy and Geochemistry* **2010**.

[51] R. Rizzo, S. Gupta, M. Rogowska, R. Ambat, *Corros. Sci.* **2020**, *162*, 108214.

[52] A. Dugstad, *Corrosion* **2006**, *61*, 1.

[53] W. Sun, S. Nešić, R. C. Woollam, *Corros. Sci.* **2009**, *51*, 1273.

[54] J. Han, S. Nešić, Y. Yang, B. N. Brown, *Electrochim. Acta* **2011**, *56*, 5396.

[55] R. De Motte, E. Basilico, R. Mingant, J. Kittel, F. Ropital, P. Combrade, S. Necib, V. Deydier, D. Crusset, S. Marcelin, *Corros. Sci.* **2020**, *172*, 108666.

[56] A. V. Syugaev, N. V. Lyalina, S. F. Lomaeva, S. M. Reshetnikov, *Prot. Met. Phys. Chem. Surf.* **2012**, *48*, 515.

[57] F. Mercier-Bion, J. Li, H. Lotz, L. Tortech, D. Neff, P. Dillmann, *Corros. Sci.* **2018**, *137*, 98.

[58] M. Saheb, D. Neff, C. Bataillon, E. Foy, P. Dillmann, *Corros. Sci.* **2011**, *53*, 2201.